sustainability

MDPI

Article

Uneven Fisheries Observability Across the Western Pacific: Implications of Nighttime Light–AIS Integration for Sustainable Fisheries Monitoring

Lei Chen [1], Chun Wang [2], Guangyuan Liu [2], Zhenxiang Ling [2], Zheng Cao [2], Qifei Zhang [2], Zhifeng Wu [2], Zhicheng Yang [3] and Zihao Zheng [2,*]

[1] Technology Innovation Center for South China Sea Remote Sensing, Surveying and Mapping Collaborative Application, Ministry of Natural Resources, Guangzhou 510310, China; chenlei@scs.mnr.gov.cn

[2] School of Geography and Remote Sensing, Guangzhou University, Guangzhou 510006, China; wangchun@e.gzhu.edu.cn (C.W.); 2112201049@e.gzhu.edu.cn (G.L.); lingzx@e.gzhu.edu.cn (Z.L.); jnczdl@gzhu.edu.cn (Z.C.); zhangqf@gzhu.edu.cn (Q.Z.); zfwu@gzhu.edu.cn (Z.W.)

[3] Institute of Biology and Environmental Science, Carl von Ossietzky Universität Oldenburg, 26129 Oldenburg, Germany; zhicheng.yang@uni-oldenburg.de

* Correspondence: zhengzh@gzhu.edu.cn

Abstract

Background: Public AIS data may represent light-attracted fisheries unevenly across coastal regions, whereas VIIRS–DNB provides a complementary optical observation of bright offshore activity. **Aims**: We develop a regional framework to compare VIIRS-derived fishing-light patterns with AIS-derived vessel activity and to compare model-inferred environmental associations between East Asian and Southeast Asian coastal waters. **Methods**: Monthly VIIRS–DNB composites, GFW AIS-derived fishing effort and gear categories, and monthly CMEMS sea-surface temperature (SST), sea-surface height (SSH), sea-surface salinity (SSS), surface-current velocities, dissolved oxygen (DO), mixed-layer depth (MLD), and chlorophyll-a (Chl-a) were harmonized for 2017–2020. VIIRS detections were screened for coastal and fixed-light contamination, and spatial density, temporal correlation, spatial-error model (SEM), Geodetector, and MaxEnt analyses were applied. **Results**: East Asia showed more continuous high-intensity fishing-light belts with summer–autumn peaks, whereas Southeast Asia showed more fragmented activity with a stronger spring peak. In Southeast Asia, squid-jigging activity had the closest spatial correspondence among AIS categories and strong temporal synchronization with fishing-light intensity (Spearman's r_s = 0.890, $p < 0.001$), but its spatial explanatory power remained limited (q = 7.8%, $p < 0.001$). Within the selected predictor set, SST had the highest model-derived contribution in East Asia, whereas SSS had the highest model-derived contribution in Southeast Asia; these results represent model-inferred environmental associations rather than causal effects. **Conclusions and recommendations**: Regional contrasts describe VIIRS-derived fishing-light patterns, whereas differences in AIS correspondence indicate potential observation gaps but may also reflect fleet composition, vessel-light intensity, and genuine differences in fishing activity. We recommend combining optical and tracking observations and reporting uncertainty from AIS coverage, VIIRS detection limits, spatial sampling, and environmental-model assumptions.

Keywords: nighttime-light remote sensing; VIIRS–DNB; Automatic Identification System (AIS); fishing-light intensity; light-attracted fisheries; fisheries monitoring; coastal surveillance; oceanographic variables

Check for updates

Academic Editors: Mustapha Aksissou, Mghili Bilal and Hesham Awadh

Received: 23 July 2026
Revised: 23 August 2026
Accepted: 28 August 2026
Published: 30 August 2026

1. Introduction

Monitoring light-attracted fisheries remains challenging in many coastal waters because a substantial share of fishing activity is mobile, weakly reported, and unevenly represented in conventional vessel-tracking systems [1]. Here, fisheries observability denotes the degree to which publicly available AIS observations represent the spatial and temporal patterns of VIIRS-derived fishing-light activity. This observability gap limits efforts to compare fisheries across regions and to identify where remotely sensed signals capture activity that public tracking data do not. In the western Pacific, where industrialized temperate fisheries and tropical small-scale fisheries coexist, the key challenge is therefore not only to map fishing activity, but also to evaluate how well different observation systems represent it.

Conventional monitoring sources do not observe the same portion of fishing activity. Logbooks depend on timely and accurate reporting and may differ in coverage and standards among jurisdictions [2]. AIS provides trajectory and vessel-attribute information [3,4], but it is more complete for vessels that carry and transmit the relevant equipment, so smaller vessels or vessels with interrupted transmission may be underrepresented [5,6]. VIIRS–DNB observes radiance rather than vessel identity and can therefore complement AIS [7,8], but it is affected by detection thresholds, spatial resolution, cloud and lunar contamination, and non-fishing lights [9]. These differences motivate a cross-source assessment rather than direct substitution of one system for another.

Recent studies have demonstrated that integrating AIS trajectories with nighttime-light imagery not only helps identify untracked vessel activity through spatial matching, but also allows for the quantification of fishing intensity and the discrimination of vessel types by leveraging the complementary strengths of both data sources [10–12]. Such multi-source data fusion approaches provide a novel technical pathway for disentangling the complexity of both coastal and distant-water fishing activities.

Although nighttime-light remote sensing has been applied in the Sea of Japan, the South China Sea, and the Indian Ocean [13–15], most studies focus on individual regions, and cross-regional comparisons of fishing-light patterns remain limited. Studies of environmental variables have also produced region-specific findings, but it remains unclear whether the predictors receiving the highest model-derived contributions differ between temperate and tropical coastal systems [16,17]. The western Pacific provides a useful comparative setting because East Asian and Southeast Asian coastal waters differ in climate, geography, fleet organization, management context, and available observation coverage. Preliminary evidence suggests that temperature-related variables may be more informative in East Asia whereas hydrological variables may be more informative in Southeast Asia [16–18]. These contrasts motivate a cross-regional analysis, while the relative contribution of climate, fleet organization, management, and observation coverage is not estimated directly here.

The novelty of this study lies in treating fisheries observability as a cross-source measurement problem. Rather than using VIIRS–DNB only to map fishing lights or AIS only to map tracked vessels, we compare their spatial, temporal, and explanatory correspondence and then examine model-inferred environmental associations separately by region. This design compares potential observation gaps with differences in remotely sensed fishing-light patterns and provides a transferable diagnostic workflow for data-sparse coastal systems.

To implement this design, we integrate VIIRS–DNB nighttime-light data, AIS trajectories, and oceanographic datasets across East Asian and Southeast Asian coastal waters. Specifically, this study addresses the following research questions:

(1) RQ1: Where do VIIRS-derived fishing-light patterns reveal persistent light-attracted fishing activity in East Asia and Southeast Asia?

(2) RQ2: Where does AIS-based vessel activity align with, or underrepresent, VIIRS-derived fishing-light observations?

(3) RQ3: How do model-inferred environmental associations of remotely sensed fishing activity differ between temperate and tropical coastal systems?

2. Materials and Methods

2.1. Study Area: Western Pacific Coastal Waters

The study area extends approximately from 91° E to 145° E and from 25° S to 60° N, covering western Pacific coastal waters with substantial light-attracted fishing activity (Figure 1). For comparative analysis, the study area was divided into two subregions according to latitude and geographic and hydrographic setting. This division provides a consistent framework for regional comparison and does not assume that observed differences are caused by fisheries management, fleet composition, or AIS coverage:

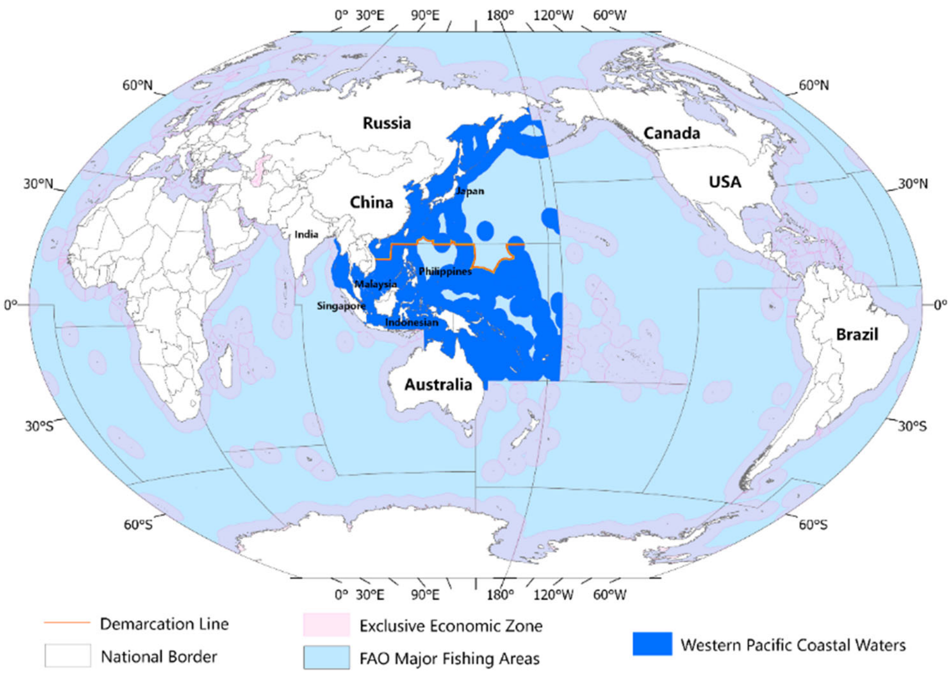

Figure 1. Overview of the study area showing the western Pacific coastal waters of East Asia and Southeast Asia.

(1) East Asia (temperate waters), including the Sea of Japan, the Yellow Sea, and the East China Sea. This subregion represents the temperate portion of the study domain and is influenced by monsoon circulation and interactions between warm and cold currents.

(2) Southeast Asia (tropical waters), including the South China Sea and the waters of the Indonesian Archipelago. This subregion represents the tropical portion of the study domain and is characterized by monsoon circulation and complex archipelagic geography.

Specifically, FAO Major Fishing Areas 61 (Northwest Pacific) and 71 (Western Central Pacific) were selected as the primary spatial units [19]. These boundaries were further refined using the global Exclusive Economic Zone (EEZ) dataset obtained from Marine Regions (https://www.marineregions.org/downloads.php, accessed on 28 August 2026) and the spatial clustering characteristics of light-attracted fishing activity, resulting in a final study extent of 91° E–145° E and 25° S–60° N. This spatial delineation excludes distant-water fishing grounds in the open Pacific dominated by the North Pacific Current, thereby focusing the analysis on western Pacific coastal waters shaped by monsoonal forcing and complex land–sea interactions.

2.2. Data Sources and Data Preprocessing

This study constructed a multi-source dataset integrating nighttime-light remote sensing, AIS-derived fishing activity data, and oceanographic environmental variables, with the analysis period spanning 2017–2020. This temporal window was selected to build a complete four-year monthly panel under a consistent processing framework across VIIRS–DNB nighttime-light composites, GFW AIS-derived fishing activity data, and CMEMS environmental variables. The period also avoids the relatively sparse pre-2016 AIS coverage and provides sufficient monthly observations for seasonal, interannual, and cross-regional comparisons.

2.2.1. Nighttime-Light Imagery (VIIRS–DNB)

Nighttime-light remote-sensing data were obtained from the Day/Night Band (DNB) of the Visible Infrared Imaging Radiometer Suite (VIIRS) onboard the Suomi National Polar-orbiting Partnership (Suomi NPP) satellite. The VIIRS–DNB sensor acquires global nighttime observations in the visible and near-infrared spectrum (400–900 nm) with a spatial resolution of 15 arc-seconds (approximately 500 m), and the original radiance values are expressed in units of $nW \cdot cm^{-2} \cdot sr^{-1}$. Compared with earlier DMSP/OLS data, VIIRS–DNB exhibits a substantially enhanced capability for detecting low-intensity light sources and anthropogenic illumination [8], making it particularly suitable for monitoring light-attracted fishing activities. However, VIIRS–DNB detects radiance rather than vessel identity, and its detection capability depends on vessel-light intensity, background conditions, and the selected threshold; the approximately 500 m spatial resolution also limits the separation of nearby or mixed light sources.

In this study, a total of 48 monthly composite VIIRS–DNB images from 2017 to 2020 were employed. The selection of monthly composites over daily records was a deliberate methodological choice to enhance the spatial signal-to-noise ratio. In the monsoon-dominated western Pacific, daily DNB data are frequently compromised by transient cloud cover and varying lunar illumination. This temporal aggregation is consistent with the monthly CMEMS oceanographic variables used for MaxEnt modeling of environmental associations. Our focus is on seasonal/interannual and cross-regional contrasts rather than day-to-day fishing events. The data were obtained from the Earth Observation Group (EOG) of the National Geophysical Data Center (NGDC) and correspond to stray-light-corrected monthly products in which observations affected by lightning, moonlight, and cloud cover were screened or reduced during product generation, although residual contamination may remain. To enhance fishing-related light signals and reduce background noise and non-fishing light contamination, a series of multi-step preprocessing procedures was applied, following and extending the approaches proposed by Elvidge et al. [8] and Li et al. [9]:

(1) Coastal light masking: a 4 km seaward buffer was selected empirically and applied along the coastline to reduce light spillover from coastal cities and ports.

(2) Removal of offshore infrastructure lights: fixed light sources associated with offshore oil and gas platforms were excluded based on existing-platform distribution datasets.

(3) Radiometric enhancement and noise suppression: image pixels were rescaled, restricted to positive values, and log-transformed to enhance the contrast between fishing vessel lights and background signals. Subsequently, a 3×3 median filter and the Spike Median Index (SMI) filter were applied to enhance the structural integrity of fishing light features while suppressing random noise.

(4) Threshold determination and cross-source checking: A radiance threshold of $1.2\ nW \cdot cm^{-2} \cdot sr^{-1}$ was selected empirically from the image histograms. The resulting

detections were then compared with the spatial distribution of AIS-derived fishing-effort grid cells as a cross-source consistency check.

To further eliminate spurious signals, extremely bright outliers exceeding three standard deviations above the mean radiance were removed to exclude high-energy particle interference. The final set of VIIRS-derived light detections was converted into point features for subsequent spatiotemporal analyses and MaxEnt modeling of environmental associations.

2.2.2. AIS-Derived Fishing Effort Data

AIS-derived apparent fishing effort data were obtained from Global Fishing Watch (GFW) [4]. The dataset used in this study consisted of daily fishing-effort records provided on a 0.01° grid and classified by flag state and GFW gear-type label, with fishing effort measured in hours. The analysis was restricted to 2017–2020 to construct a consistently processed four-year monthly panel aligned with the VIIRS–DNB nighttime-light composites and CMEMS oceanographic variables used in this study.

Each record contained the date, grid-cell coordinates, flag state, gear-type label, and fishing hours. AIS-derived fishing-effort data can be used to characterize spatial fishing patterns and support fishing-ground identification, including when vessel-type information is incomplete [20]. Records with zero fishing hours were removed using Python and SQL-based workflows. The GFW gear-type labels were then harmonized into five analytical categories: gillnet, longline, purse seine, squid jigging, and trawl, following established fishing-gear classifications [21]. The detailed mapping between the original GFW gear labels and these analytical categories is provided in Table 1. Squid-jigging vessels were given particular attention because of their relevance to light-attracted fishing activities. These categories represent AIS-derived gear-type groupings and do not imply one-to-one identification of the vessel responsible for an individual VIIRS detection.

Table 1. AIS-based classification of fishing-vessel types used in this study.

Original Gear Type (GFW)	Classified Vessel Type
set_longlines, drifting_longlines	Longline
seines, purse_seines, other_seines, other_purse_seines, tuna_purse_seines	Purse seine
squid_jigger	Squid jigging
trawlers, dredge_fishing, trollers	Trawl
set_gillnets	Gillnet

2.2.3. Marine Environmental Data

Marine environmental factors are key variables influencing the spatial distribution and intensity of light-attracted fisheries. In this study, eight environmental variables were selected: sea-surface temperature (SST), sea-surface height (SSH), sea-surface salinity (SSS), zonal surface-current velocity (SSV-U), meridional surface-current velocity (SSV-V), dissolved-oxygen concentration (DO), mixed-layer depth (MLD), and chlorophyll-a concentration (Chl-a). All eight environmental variables were obtained from the Copernicus Marine Environment Monitoring Service (CMEMS) at a monthly temporal resolution and a native spatial resolution of 0.083° × 0.083° (Table 2). Before MaxEnt modeling, each continuous environmental layer was resampled to a 0.1° × 0.1° geographic grid using bilinear interpolation and exported as an ASCII raster layer. The ASCII files used −9999 as the NoData value. These variables were selected to represent thermal, saline, dynamic, oxygen, mixed-layer, and productivity conditions relevant to the spatial distribution of light-attracted fisheries.

Table 2. Overview of multi-source datasets and key variables.

Data Type	Data Source	Temporal Coverage	Spatial Resolution	Key Variables	Primary Purpose
AIS Vessel Data	Global Fishing Watch (GFW)	2017–2020	0.01° (~1 km)	Date, grid-cell coordinates, flag state, gear type, fishing hours	Classification of vessel types; generation of vessel-type fishing-effort density surfaces; assessment of AIS–VIIRS correspondence.
VIIRS–DNB	Suomi NPP VIIRS (EOG/NGDC)	2017–2020	~500 m	$nW/cm^2/sr$	Detection of fishing-vessel light sources; characterization of spatial patterns and intensity of light-attracted fishing; cross-source consistency checking against AIS-derived fishing-effort data
Environmental Data	Copernicus Marine Environment Monitoring Service (CMEMS)	2017–2020	0.083° × 0.083° native resolution; resampled to 0.1° × 0.1° for MaxEnt, monthly	SST, SSH, SSS, surface currents (U/V), DO, MLD, Chl-a	MaxEnt modeling of environmental associations and relative fishing-light occurrence potential
Auxiliary Data	FAO Major Fishing Areas; Marine Regions World EEZ dataset	Static boundary datasets	Vector boundaries	Fishing area boundaries; Exclusive Economic Zones	Definition of spatial-analysis units; delineation of coastal versus offshore regions; support for spatial statistical analyses

2.3. Analytical Framework and Methods

2.3.1. A Remote-Sensing Framework for Assessing Fisheries' Observability

The analysis followed three stages aligned with RQ1–RQ3 (Figure 2). First, monthly VIIRS–DNB composites were processed into fishing-light intensity surfaces and analyzed using kernel-density estimation, emerging spatiotemporal-hotspot analysis, and centroid migration. Second, AIS vessel categories were aggregated to the same spatial and temporal scale and compared with VIIRS-derived fishing-light intensity using SDI, SEM, Spearman's rank correlation, and Geodetector. Third, MaxEnt models used VIIRS-derived presence points and monthly oceanographic variables to compare regional environmental associations.

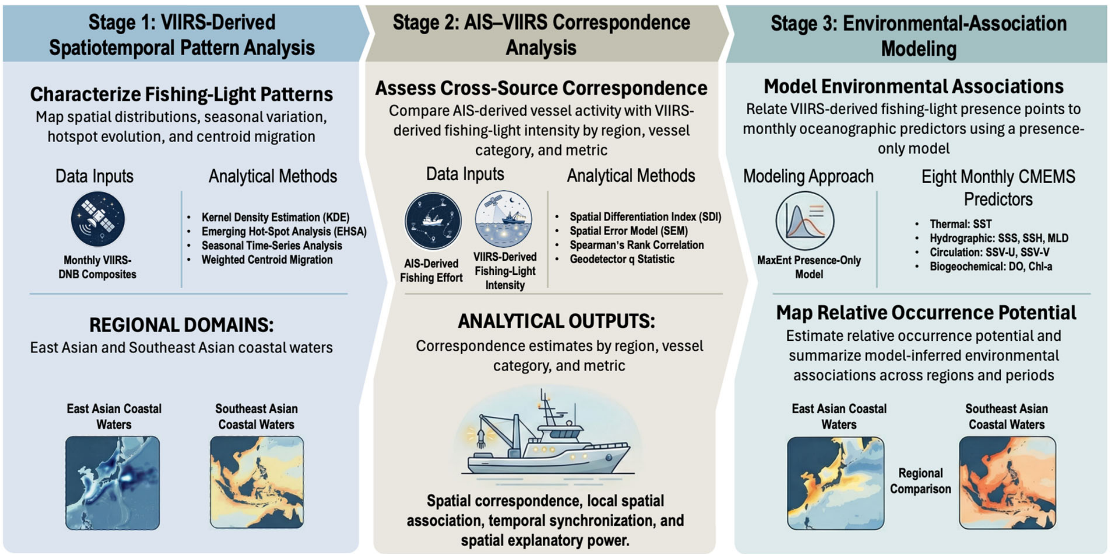

Figure 2. Analytical framework for comparing VIIRS-derived fishing-light patterns, AIS–VIIRS correspondence, and model-inferred environmental associations across East Asian and Southeast Asian coastal waters. Stage 1 characterizes spatiotemporal fishing-light patterns; Stage 2 evaluates spatial and temporal correspondence between AIS-derived vessel activity and VIIRS-derived fishing-light intensity; and Stage 3 estimates environmental associations and relative occurrence potential using MaxEnt.

2.3.2. VIIRS-Derived Spatiotemporal Pattern Analysis

Monthly VIIRS-derived fishing-light intensity was analyzed on a 0.1° grid using KDE, EHSA based on Getis-Ord Gi* and the Mann–Kendall test, and weighted centroid migration. AIS-derived fishing-effort grids were processed using KDE on the same 0.1° output grid for the subsequent AIS–VIIRS correspondence analyses.

(1) **Kernel Density Estimation, KDE**

To place the VIIRS and AIS-derived observations on a common spatial support, kernel density estimation (KDE) [22] was used to generate continuous fishing-light brightness (FLB) and fishing-track density (FTD) surfaces from VIIRS-derived light detections and 0.01° AIS fishing-effort records, respectively. A quartic kernel was applied, with VIIRS radiance and AIS fishing hours used as input weights for the two corresponding density surfaces. The kernel density estimator is defined as:

$$D(s) = \frac{1}{h^2}\sum_{i=1}^{n}\left(\frac{3}{\pi}\right)\left(1-\left(\frac{d(s,s_i)}{h}\right)^2\right)^2, d(s,s_i) < h \tag{1}$$

where s denotes the spatial location, h is the KDE bandwidth, and $d(s,s_i)$ is the distance between location s and point s_i. The bandwidth was set to 0.05°, based on the approximate maximum hourly displacement implied by the mean speed of vessels during fishing operations. The resulting fishing-track density (FTD) and fishing-light brightness (FLB) surfaces were generated on a common 0.1° grid. This common grid was used as the spatial support for the subsequent SDI, SEM, and Geodetector analyses.

(2) **Emerging Hot-Spot Analysis**

To identify the spatiotemporal evolution of light-attracted fishing intensity in East Asia and Southeast Asia, this study employed Emerging Hot-Spot Analysis (EHSA). This method is based on the Getis-Ord Gi* statistic [23] to detect local spatial clustering patterns and integrates temporal trend tests to classify hotspot evolution types. The core spatial statistic is defined as:

$$G_i^* = \frac{\sum_j w_{ij}x_j - \overline{X}\sum_j w_{ij}}{S\sqrt{\frac{n\sum_j w_{ij}^2 - (\sum_j w_{ij})^2}{n-1}}} \tag{2}$$

where x_j denotes the observed value at spatial unit j, w_{ij} represents the spatial weight between units i and j, and $\overline{X}$ and S are the global mean and standard deviation, respectively. A significantly positive G_i^* value indicates that location i and its neighboring units form a hot spot, whereas a significantly negative value identifies a cold spot.

Along the temporal dimension, EHSA treats the sequence of G_i^* statistics across successive time slices as input and applies the Mann–Kendall trend test [24] to detect monotonic temporal trends.

(3) **Centroid Migration Model**

The centroid migration trajectory model is used to identify spatiotemporal variations in weighted activity centers. In this study, the model was applied to quantify temporal changes in the centroid of light-attracted fishing activities across fishing grounds. The centroid coordinates for year i were calculated as follows:

$$X_i = \frac{\sum_{j=1}^{n}(C_{i,j} \times X_{i,j})}{\sum_{j=1}^{n} C_{i,j}}, Y_i = \frac{\sum_{j=1}^{n}(C_{i,j} \times Y_{i,j})}{\sum_{j=1}^{n} C_{i,j}} \tag{3}$$

where X_i and Y_i denote the longitude and latitude of the centroid of light-attracted fishing activities in year i; $X_{i,j}$ and $Y_{i,j}$ represent the longitude and latitude of the j-th light-attracted fishing unit in year i; $C_{i,j}$ is the corresponding fishing intensity (e.g., fishing-light brightness) of that unit; and n is the total number of light-attracted fishing units in year i.

2.3.3. AIS Representativeness and Vessel-Type Attribution

AIS representativeness was assessed by comparing vessel-type activity with VIIRS-derived fishing-light intensity using spatial-pattern matching, spatial-error modeling, temporal correlation, and Geodetector.

(1) **SDI-based Spatial-Pattern-Matching Analysis**

For AIS–VIIRS correspondence analyses, the daily 0.01° AIS fishing-effort records were aggregated into monthly totals by grid cell and vessel category. Weighted KDE, using fishing hours as the weight, was then applied to each vessel category listed in Table 1 to generate vessel-activity intensity surfaces $V_k(x, y, t)$ on the common 0.1° output grid. In parallel, the monthly VIIRS-derived fishing-light detections were processed using the same KDE framework to generate corresponding fishing-light intensity surfaces $L(x, y, t)$. Therefore, AIS–VIIRS comparisons were conducted using corresponding monthly 0.1° cells from the two KDE surfaces. The Spatial Differentiation Index (SDI) was introduced to quantify the degree of spatial overlap and divergence between vessel-track density (FTD) and fishing-light brightness (FLB) [25], thereby comparing the spatial correspondence of different AIS-observed vessel categories with VIIRS-derived fishing-light patterns.

$$SDI_{i,j} = 1 - \frac{Count\left(FLB_i \cap FTD_{i,j}\right)}{Count\left(FLB_i \cup FTD_{i,j}\right)} \tag{4}$$

where FLB_i denotes the gridded light-attracted fishing intensity in the i-th marine region, and $FTD_{i,j}$ represents the trajectory density grid of the j-th vessel type in the same region.

(2) **Spatiotemporal Correlation Analysis**

Building on the spatial pattern matching analysis, the statistical association between fishing activity intensity and nighttime-light brightness was further examined in a spatiotemporal context. Given the pronounced spatial autocorrelation and spillover effects in fishing activities, in which fishing intensity in one grid cell is influenced by neighboring cells, an SEM was employed to explicitly account for spatial dependence in the residuals and to estimate the spatial association between FTD and light-attracted FLB [26]:

$$y = \beta x + \lambda W\varepsilon + \mu \tag{5}$$

where y denotes light-attracted FLB, x represents FTD, λ is the spatial error coefficient, and $W\varepsilon$ is the spatially lagged error term. Temporal synchronization between monthly vessel-track density and fishing-light intensity was quantified using Spearman's rank correlation coefficient. The calculations were performed in IBM SPSS Statistics 27.

(3) **Contribution Quantification Based on the GD Model**

Finally, this study applied the factor detector module of Geodetector to quantify the spatial explanatory power of AIS-derived vessel-density factors for VIIRS-derived fishing-light brightness on the common 0.1° analysis grid [27]. The analysis was conducted separately for each vessel category and regional domain. Within each regional domain, the VIIRS-derived fishing-light brightness and the FTD of each vessel category were ordered by intensity and reclassified into ten ordinal classes (1–10). The resulting regional ten-level layers were then used as the input variables for the factor detector. The q statistic summarizes the reduction in within-stratum variance of fishing-light brightness relative to its overall variance; larger q values indicate stronger spatial explanatory power of the corresponding vessel-density factor. The significance levels reported in Table 3 were taken from the output of the same Excel-based GeoDetector implementation.

$$q = 1 - \frac{\sum_{h=1}^{L} N_h \sigma_h^2}{N\sigma^2} \tag{6}$$

where h denotes a non-empty stratum of the regional vessel-density factor, L is the number of non-empty strata among the ten ordinal classes, N_h is the number of grid cells in stratum h, N is the total number of grid cells included in the calculation, σ_h^2 is the within-stratum variance of the corresponding fishing-light brightness response, and σ^2 is its overall variance. The q statistic ranges from 0 to 1, with larger values indicating stronger explanatory power of the vessel-density strata for the spatial stratification of fishing-light brightness.

Table 3. AIS representativeness and vessel-type attribution for VIIRS-derived fishing-light intensity in the western Pacific.

Region	Vessel Type	SDI	SEM Coefficient	Spearman's r_s	Geodetector q
East Asia	Squid jigging	0.679	80.843 ***	0.763 ***	2.5% ***
	Purse seine	0.571	0.269 ***	0.809 ***	6.1% ***
	Longline	0.834	0.103 ***	0.738 ***	1.7% ***
	Trawl	0.833	0.002	0.721 ***	2.7% ***
	Gillnet	0.609	0.015	0.728 ***	1.1% ***
Southeast Asia	Squid jigging	0.326	21.775 ***	0.890 ***	7.8% ***
	Purse seine	0.976	−0.004	0.149	1.5% ***
	Longline	0.998	0.013	0.757 ***	2.3% ***
	Trawl	0.873	0.053	0.573 ***	<0.1%
	Gillnet	-	-	-	<0.1%

Note: *** $p < 0.001$. SDI (Spatial Differentiation Index): Lower values indicate higher spatial consistency between vessel trajectories and light-attracted fishing patterns. SEM (Spatial Error Model): Coefficients represent spatial associations between vessel-track density and fishing-light intensity after accounting for spatial dependence. Spearman's r_s: Assesses the temporal synchronization of seasonal variations. Geodetector q: Represents the explanatory power of a vessel-density factor for the spatial stratification of fishing-light intensity. These metrics describe complementary dimensions of AIS–VIIRS correspondence and were therefore interpreted jointly rather than as interchangeable estimates of a single relationship. "-" indicates insufficient data samples for calculation in the region.

2.3.4. MaxEnt Modeling of Associations Between Fishing-Light Occurrence and Environmental Variables

MaxEnt was used to model environmental associations of VIIRS-derived fishing-light occurrence under a presence-only design [28,29]. High-radiance VIIRS-derived fishing-light points were used as presence points, while background points and eight monthly oceanographic variables were supplied as 0.1° × 0.1° ASCII raster layers to characterize the environmental background space. The continuous CMEMS layers were resampled from their native 0.083° × 0.083° resolution using bilinear interpolation before model fitting. All eight variables were retained as complementary predictors. No separate correlation- or VIF-based screening was applied before model fitting, so variable contributions were interpreted jointly within the selected predictor set.

Presence points were selected from the final VIIRS-derived fishing-light point features retained after the preprocessing procedures described in Section 2.2.1, including threshold screening, removal of extreme radiance outliers, and conversion to point features. The presence points were matched to the corresponding monthly environmental layers on the common 0.1° analysis grid. MaxEnt background samples were drawn from the corresponding regional modeling extent.

To account for regional heterogeneity, a multi-scenario modeling strategy was adopted by stratifying the analysis by region (East Asia vs. Southeast Asia) and period (peak vs. non-peak fishing periods). The model was implemented using MaxEnt version 3.4.1. In each run, 75% of the presence samples were randomly selected for training and the remaining 25% were held out for validation; this random partitioning was repeated ten times. Outputs were generated in logistic format and interpreted as relative occurrence potential under the selected environmental predictors.

Model performance was evaluated using the area under the receiver operating characteristic curve (AUC), calculated from the 25% held-out validation subset [30]. AUC values were interpreted relative to the random expectation of 0.5, with higher values indicating stronger discrimination between presence and background conditions. Because AUC assesses discrimination between presence and background points but not spatial agreement, we additionally calculated a matching rate. MaxEnt logistic outputs were classified into five relative occurrence-potential levels using the Jenks natural-breaks method, and the upper-three classes were defined as high-potential zones (HPZs). The matching rate was calculated as:

$$MatchingRate = \frac{N_{HPZ}}{N_{total}} \times 100\% \tag{7}$$

where N_{HPZ} is the number of observed fishing points located within HPZs and N_{total} is the total number of observed fishing points. A higher matching rate indicates greater within-region overlap between model-inferred HPZs and observed fishing-light locations. The metric was used as a descriptive measure of model–observation agreement rather than as a formal test of differences between regions.

To attribute environmental variables, jackknife tests and response curve analyses were conducted. The jackknife approach, together with percent contribution and permutation importance metrics, was used to quantify the relative contributions of individual environmental variables to model gain. Response curves were then examined to characterize modeled nonlinear response patterns and to identify environmental ranges associated with higher occurrence probabilities of light-attracted fishing activity.

2.3.5. Software and Reproducibility

Data preprocessing was implemented in Python 3.12 using SQL-based workflows. Kernel density estimation was conducted in ArcGIS Pro 3.3. Spatial-error models were fitted in OpenGeoDa 1.22.0, and temporal synchronization was assessed using Spearman's rank correlation in IBM SPSS Statistics 27. Geodetector q statistics were calculated using the official Excel-based GeoDetector implementation. MaxEnt version 3.4.1 was used to model associations between VIIRS-derived fishing-light occurrence and the selected environmental variables. The main spatial resolutions, training-validation split, and replicate settings are reported in Sections 2.3.1–2.3.4.

3. Results

3.1. VIIRS-Derived Spatiotemporal Patterns of Fishing-Light Activity

3.1.1. Spatial Distribution Patterns

Satellite observations indicated a pronounced nearshore concentration of light-attracted fishing in the western Pacific marginal seas, with clear regional differences in spatial organization (Figure 3a,b). East Asian waters showed more continuous and intensive distributions, whereas Southeast Asian waters exhibited more fragmented and dispersed patterns.

https://doi.org/10.3390/su18178881

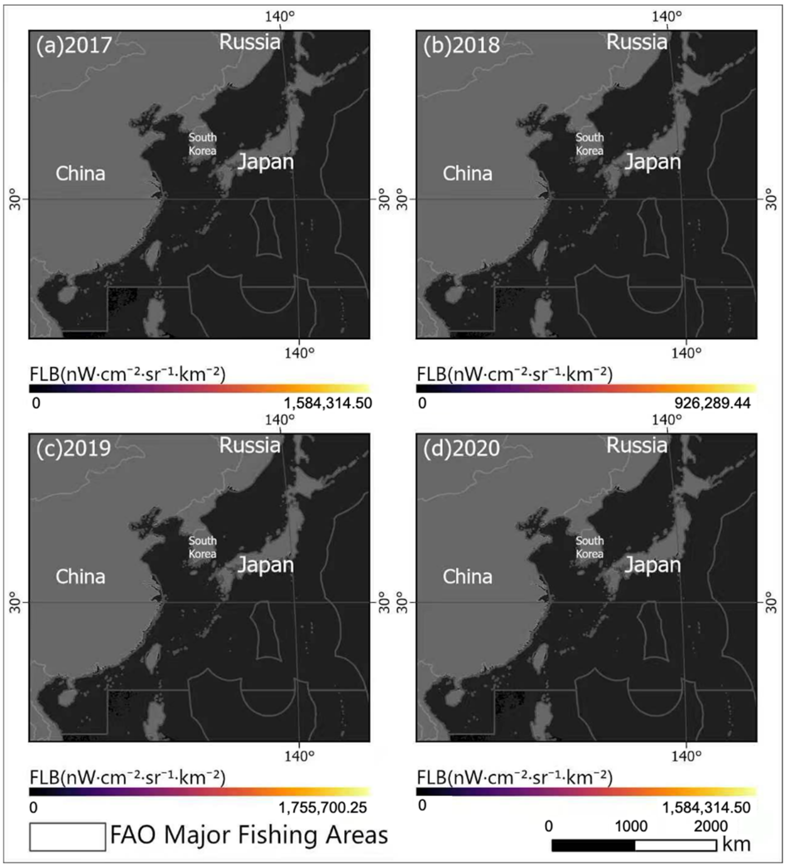

(**a**)

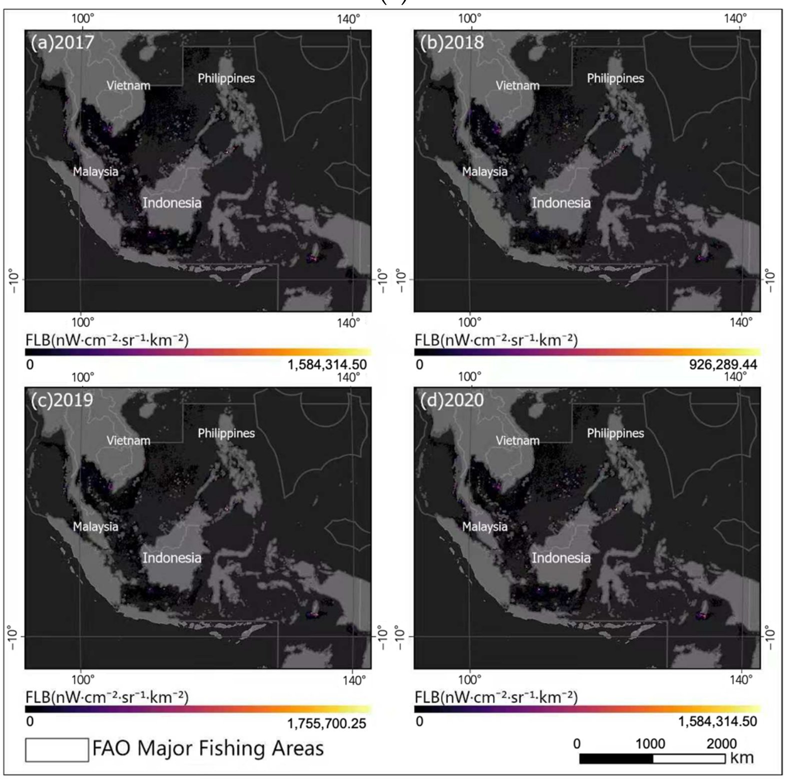

(**b**)

Figure 3. *Cont.*

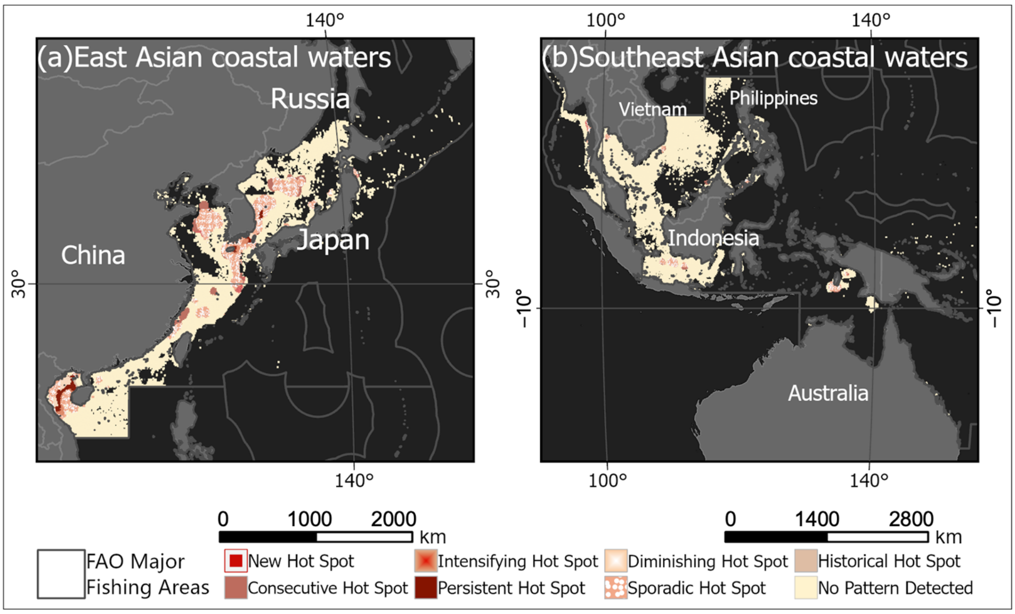

(**c**)

Figure 3. (**a**). Kernel density maps of fishing light brightness (FLB) in East Asian coastal waters (2017–2020). (**b**). Kernel density maps of fishing light brightness (FLB) in Southeast Asian coastal waters (2017–2020). (**c**). Emerging Hot-Spot Analysis (EHSA) of light-attracted fishing activity across East Asia and Southeast Asia (2017–2020).

In East Asian coastal waters, light-attracted fishing formed a high-intensity, continuous belt extending from the Beibu Gulf and the East China Sea through the Yellow Sea and the Sea of Japan. This region accounted for approximately 50% of the detected FLB intensity, with particularly dense clusters in the East China Sea–Yellow Sea transition zone and the Sea of Japan.

Southeast Asian coastal waters showed multi-centered and patchy distributions, with major concentrations around the southern Indochina Peninsula, the Java Sea, and the Arafura Sea. Local FLB density was generally lower and more fragmented than in East Asia. EHSA further indicated more persistent or intensified hotspots in East Asia, compared with more scattered and intermittent hotspot signals in Southeast Asia (Figure 3c).

3.1.2. Seasonal and Interannual Variations

At the aggregate scale, the annual time series shows an apparent double-peak/double-trough pattern (Figure 4). This pattern reflects different seasonal phases between the two subregions: East Asian coastal waters show a later summer–autumn maximum, whereas Southeast Asian waters show an earlier spring maximum and stronger month-to-month variability. The earlier Southeast Asian peak and later East Asian peak produce two elevated periods in the combined annual curve, with lower activity between them.

In East Asian coastal waters, fishing intensity remained relatively low during January–April, increased from May onward, and reached its main peak during August–November before declining rapidly after December. In contrast, Southeast Asian coastal waters showed stronger fluctuations, with a primary peak during March–May. After 2019, the temporal pattern became more multi-peaked and oscillatory. The observed seasonal peak was later in East Asia, occurring mainly in summer–autumn, and earlier in Southeast Asia, occurring mainly in spring (Figure 4).

Overall, the two subregions exhibited a seasonal phase offset, with peak activity occurring mainly in summer–autumn in East Asia and in spring in Southeast Asia. Given the repeated monthly structure of the 48-month series and the potential dependence among observations, this phase offset is reported as a descriptive regional contrast rather than a formally tested difference.

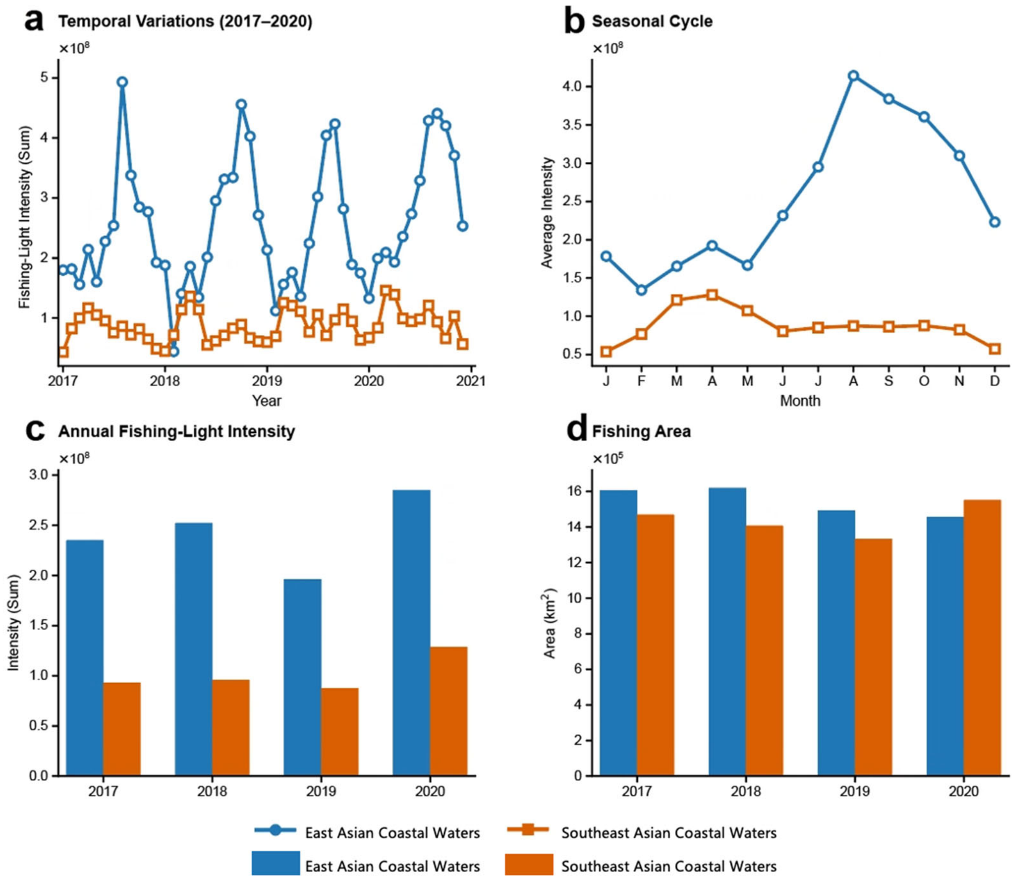

Figure 4. Temporal, seasonal, and annual variation in light-attracted fishing activity in East Asian and Southeast Asian coastal waters, 2017–2020. (**a**) Monthly fishing-light intensity; (**b**) four-year mean seasonal cycle; (**c**) annual fishing-light intensity; and (**d**) annual fishing area. Blue and orange indicate East Asian and Southeast Asian coastal waters, respectively.

3.1.3. Centroid Migration and Spatiotemporal Trends

The centroid migration model captures the spatiotemporal evolution of light-attracted fishing hotspots. Overall, the centroid of light-attracted fishing activities in the western Pacific marginal seas exhibits strong nearshore stability, with relatively small migration amplitudes that mainly reflect fine-scale adjustments within regional waters. However, clear differences in migration direction and magnitude are observed between East Asia and Southeast Asia (Figure 5).

In East Asian coastal waters, the centroid of light-attracted fishing activities shows a gradual southwestward shift. From 2017 to 2020, the centroid migrated from the nearshore waters off Zhoushan, Zhejiang Province (122°16′ E, 29°58′ N) to the coastal waters off Sanmen, Taizhou (121°39′ E, 29°12′ N), with a cumulative displacement of approximately 104 km, indicating a consistent directional movement.

In contrast, the centroid migration in Southeast Asian coastal waters is characterized by limited displacement and overall stability. Over the same period, the total centroid shift was approximately 30 km, remaining anchored near (110°10′ E, 5°43′ N). Interannual variability was observed, with a notable southeastward deviation of about 186 km in 2019, followed by a return in 2020, without forming a sustained migration trend.

Overall, centroid dynamics of light-attracted fishing activities in the western Pacific marginal seas exhibit pronounced regional differences: East Asian waters show a persistent directional migration pattern, whereas Southeast Asian waters are dominated by small-amplitude oscillations and spatial stability.

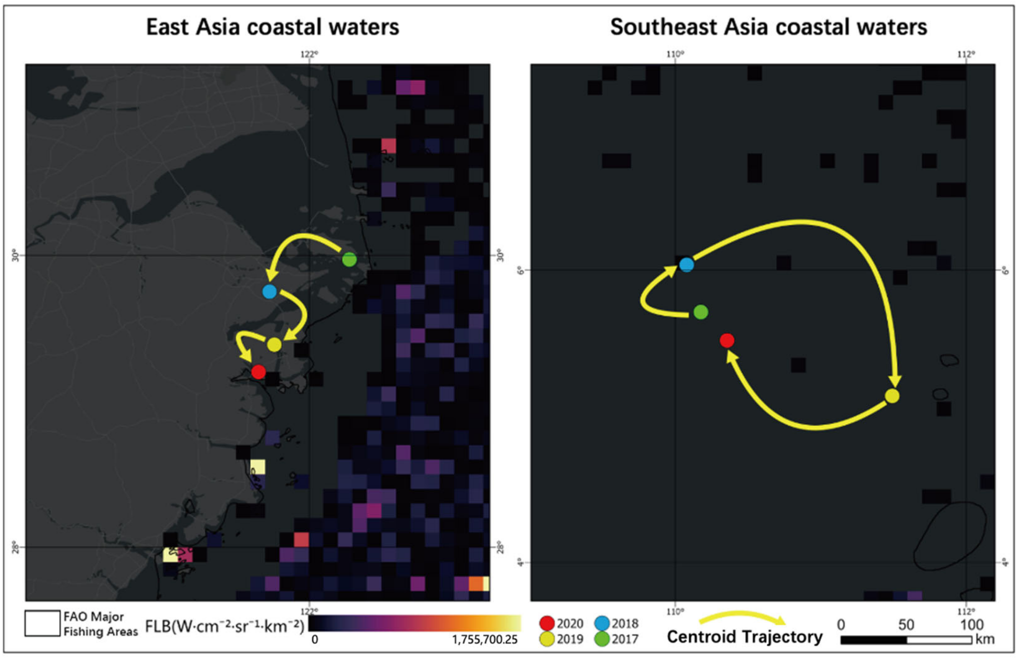

Figure 5. Interannual centroid migration of light-attracted fishing activities (2017–2020).

3.2. Regional Patterns of AIS–VIIRS Correspondence by Vessel Type

Across the western Pacific coastal waters, AIS-derived vessel activity showed region- and metric-dependent correspondence with VIIRS-derived fishing-light intensity (Table 3).

In East Asian coastal waters, purse seiners showed the closest broad-scale spatial correspondence and the highest Geodetector q value among the main vessel categories (SDI = 0.571; q = 6.1%). Squid-jigging vessels, however, had the largest positive SEM coefficient (80.843, $p < 0.001$), indicating that the leading vessel category differed across metrics.

In Southeast Asian coastal waters, squid-jigging vessels showed the closest spatial correspondence (SDI = 0.326) and a positive SEM association with fishing-light intensity (coefficient = 21.775, $p < 0.001$). Their monthly activity was also strongly synchronized with VIIRS-derived fishing-light intensity (Spearman's $r_s = 0.890$, $p < 0.001$), whereas their Geodetector explanatory power remained limited (q = 7.8%, $p < 0.001$). This contrast reflects the different dimensions captured by the two metrics: Spearman's r_s measures temporal covariation between the monthly series, whereas Geodetector q quantifies the proportion of spatial heterogeneity explained by vessel-density strata. Thus, squid-jigging activity covaried closely with fishing-light intensity over time, while squid-jigging vessel density explained only a limited share of its spatial heterogeneity.

3.3. Model-Inferred Environmental Associations and Relative Fishing-Light Occurrence Potential

3.3.1. Model Performance and Variable Importance

The MaxEnt models were evaluated for their ability to discriminate VIIRS-derived fishing-light occurrence points from background conditions in western Pacific coastal waters. ROC curves were generated separately for East Asian and Southeast Asian coastal waters during peak and non-peak periods (Figure 6a–d).

In East Asian coastal waters, mean AUC values were 0.792 during the peak period and 0.790 during the non-peak period. The corresponding mean AUC values for Southeast Asian coastal waters were 0.776 and 0.777, respectively. Variation among the ten replicate

ROC curves is shown as ±1 standard deviation in Figure 6. Overall, all four scenarios showed moderate discriminatory performance above the random expectation of 0.5.

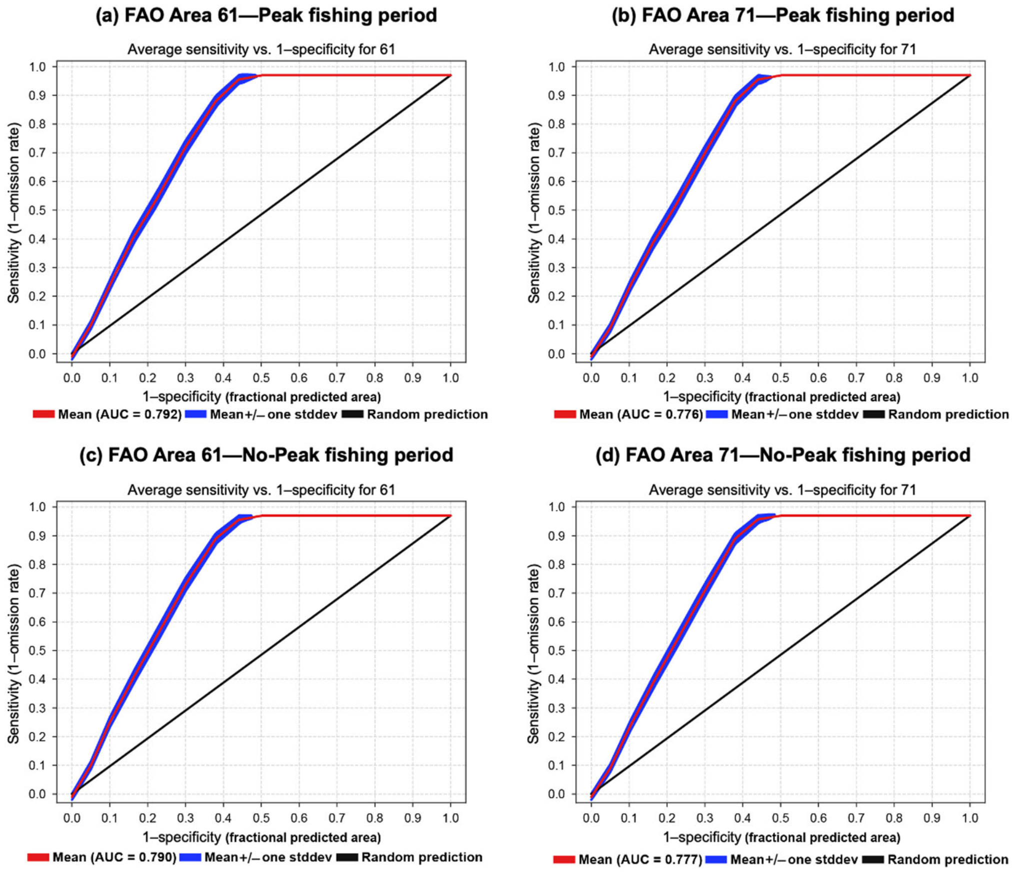

Figure 6. ROC curves and AUC values of the MaxEnt models for light-attracted fishing occurrence in FAO Areas 61 and 71 during peak and non-peak fishing periods: (**a**) Area 61, peak; (**b**) Area 71, peak; (**c**) Area 61, non-peak; and (**d**) Area 71, non-peak. Note: Red curves represent the mean ROC curves across ten replicate runs, blue envelopes indicate ±1 standard deviation, and black diagonal lines represent random prediction.

Overall, model performance was consistent but moderate across the two coastal regions. To characterize model-inferred environmental associations, jackknife results, percent contribution, and permutation importance were examined (Figure 7). The variable-importance profiles differed between regions, particularly for temperature- and salinity-related predictors.

In East Asian coastal waters, SST had the highest model-derived contribution within the selected predictor set. During the peak fishing period, SST accounted for 65.4% of the total contribution, followed by SSH (20.5%) and Chl-a (6.8%). During the non-peak period, the contribution of SST decreased to 48.6%, whereas that of Chl-a increased to 22.5%. The SST response curve showed higher modeled fishing-light occurrence potential between 16.55 and 27.78 °C, reaching a maximum at approximately 22.92 °C.

In Southeast Asian coastal waters, SSS had the highest model-derived contribution within the selected predictor set, accounting for 88.6% during the peak fishing period and 84.5% during the non-peak period. The response curves for SSS showed higher modeled fishing-light occurrence potential between 19.14 and 33.65 PSU. SST and DO made smaller model-derived contributions, accounting for 5.4% and 2.9%, respectively.

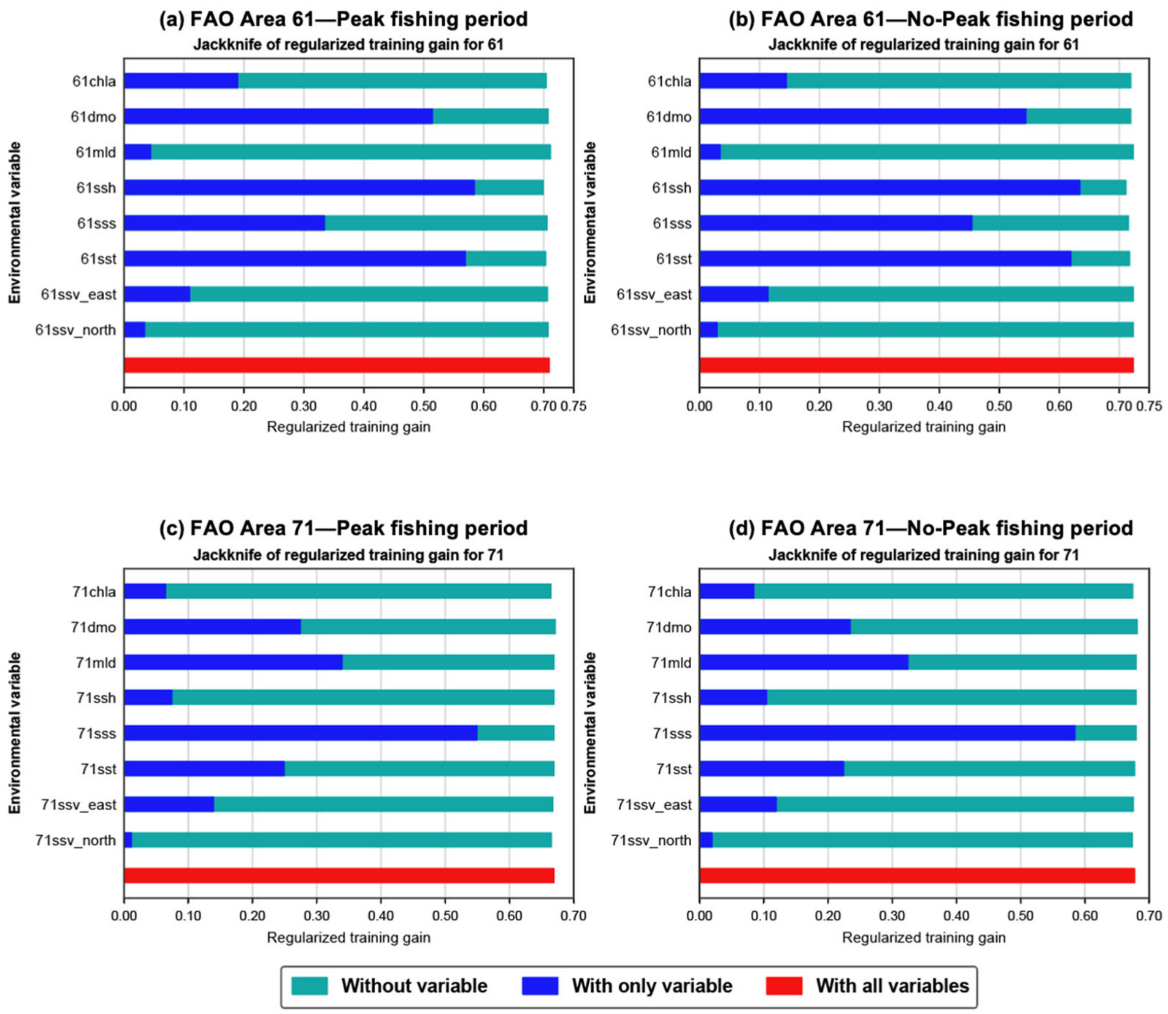

Figure 7. Jackknife analysis of environmental-variable importance in the MaxEnt models for coastal light-attracted fishing occurrence: (**a**) FAO Area 61, peak fishing period; (**b**) FAO Area 61, non-peak fishing period; (**c**) FAO Area 71, peak fishing period; and (**d**) FAO Area 71, non-peak fishing period.

3.3.2. Model-Inferred High-Potential Areas

MaxEnt predictions showed regional variation in relative fishing-light occurrence potential across western Pacific coastal waters. During both peak and non-peak periods, model-inferred high-potential zones (HPZs) were concentrated along continental shelf margins and around island-reef systems (Figure 8). The spatial configuration of these zones and their overlap with observed fishing-light locations differed between East Asian and Southeast Asian coastal waters.

In East Asian coastal waters, model-inferred HPZs formed a relatively continuous belt along the continental shelf. Of the observed fishing-light locations, 73.78% fell within these HPZs, while the remaining locations occurred in areas with lower modeled occurrence potential.

In Southeast Asian coastal waters, model-inferred HPZs were more fragmented and concentrated around the Indochina coast and the Sunda Shelf. The corresponding matching rate was 96.52%, indicating greater descriptive overlap between the HPZs and observed fishing-light locations than in East Asia under the applied classification.

Overall, the fitted models produced broader HPZs with lower descriptive overlap in East Asia and narrower HPZs with higher descriptive overlap in Southeast Asia. These matching rates summarize model-observation agreement within each region and were not used to establish a statistically significant regional difference.

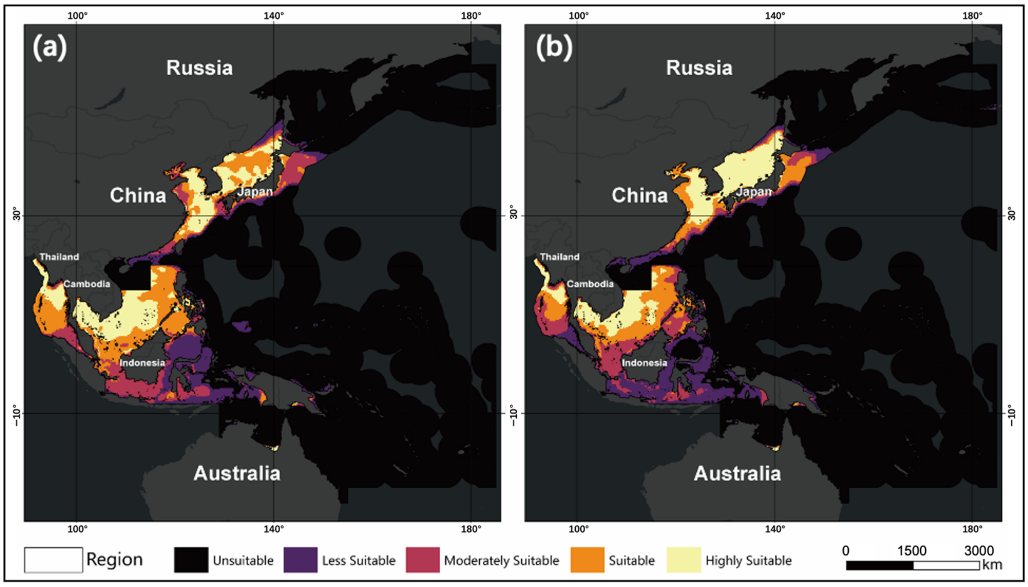

Figure 8. Model-inferred relative occurrence potential of VIIRS-derived fishing-light activity during (**a**) peak and (**b**) non-peak periods, classified into five relative levels using the Jenks natural-breaks method.

4. Discussion

4.1. Interpreting VIIRS-Derived Fisheries Patterns Across Contrasting Coastal Systems

The results of this study reveal a pronounced North–South structural divergence in light-attracted fishing activities along the western Pacific coast. East Asian waters were characterized by high-intensity, continuous belt-like patterns and summer–autumn activity, whereas Southeast Asian waters showed more fragmented distributions and a spring-dominated peak. These observations are broadly consistent with previous studies using nighttime-light imagery and vessel-tracking data to identify seasonal and spatially clustered fishing activities in the Sea of Japan, the China Seas, and other western Pacific waters [13,14,16,31]. The present study extends these observations by comparing the spatial and seasonal organization of the two coastal systems within a common analytical framework.

(1) Latitudinal Contrast in Model-Inferred Environmental Associations: Thermal vs. Salinity-Related Patterns

Previous studies have linked nighttime fishing distributions in the Northwest Pacific and the China Seas to sea-surface temperature, seasonal hydrography, and thermal-front conditions [16,32–34]. Consistent with these observations, SST had the highest model-derived contribution within the selected predictor set in East Asian coastal waters. Fishing-light occurrence was mainly concentrated within the modeled SST range of 16–28 °C. However, the present analysis identifies an environmental association rather than directly testing the biological processes responsible for the observed belt-like distribution.

In tropical Southeast Asian waters, previous studies have emphasized the roles of regional circulation, freshwater influence, and seasonal hydrographic variability in shaping fishing-ground conditions [18,35]. In our models, SSS had the highest model-derived contribution within the selected predictor set, whereas SST made a smaller relative contribution. This salinity-related association may be consistent with regional hydrological variability, although its magnitude may also be influenced by predictor dependence and the spatial distribution of presence samples.

(2) Regional Differences in Vessel-Type Correspondence and AIS Representativeness

Beyond environmental associations, AIS–VIIRS correspondence varies by vessel type and region. In East Asia, purse seiners showed closer broad-scale spatial correspondence and higher Geodetector explanatory power, whereas squid jiggers showed a larger positive SEM coefficient with fishing-light intensity. Previous AIS–VIIRS matching studies have similarly shown that nighttime-light observations and vessel-tracking data provide complementary information for vessel detection and gear-type attribution [10–12]. Our results extend this approach by showing that the vessel category with the closest correspondence may differ according to the spatial metric used.

In Southeast Asia, AIS-observed squid jiggers showed the closest spatial correspondence, but their Geodetector explanatory power remained limited at 7.8%. This pattern may reflect incomplete AIS coverage, regional fleet composition, differences between optical and tracking observations, or spatial and temporal aggregation. Previous studies have documented uneven vessel-tracking coverage and the complementary role of nighttime-light observations in detecting fishing activity that is weakly represented in AIS data [5,8–10]. The present data cannot determine which of these explanations predominates.

(3) Regional Differences in Model–Observation Agreement

Across the four modeling scenarios, mean AUC values of approximately 0.78 indicated moderate discrimination between fishing-light occurrence points and background conditions. The models were therefore used to compare broad regional environmental associations rather than to support precise site-level prediction. The matching rates describe within-region overlap between model-inferred HPZs and observed fishing-light locations. The higher rate in Southeast Asia than in East Asia (96.52% vs. 73.78%) indicates greater descriptive model–observation overlap under the applied classification. Because the occurrence locations may be spatially dependent and do not constitute independent regional replicates, these percentages were not subjected to a formal test of regional differences. The observed contrast may reflect predictor coverage, fleet composition, fishing practices, sampling characteristics, or variables not included in the models.

Overall, the three evidence streams characterize different components of the regional contrast. VIIRS–DNB showed continuous fishing-light patterns with summer–autumn peaks in East Asia and more fragmented patterns with an earlier spring peak in Southeast Asia. AIS comparisons revealed region- and metric-dependent correspondence between tracked vessel activity and VIIRS-derived fishing-light observations. MaxEnt identified SST and SSS as the highest model-derived contributions within the selected predictor set in East Asia and Southeast Asia, respectively, together with different levels of descriptive model–observation overlap. Collectively, these findings distinguish the two regions in terms of observed fishing-light patterns, cross-source correspondence, and model-inferred environmental associations, but they do not isolate the environmental, operational, or observational causes of those differences.

4.2. Implications for Remote-Sensing-Based Coastal Monitoring

The AIS–VIIRS comparison provides a way to assess uneven fisheries observability across coastal systems. The inference of potential AIS-based observation gaps is based on the joint interpretation of SDI, SEM, temporal synchronization, and Geodetector q rather than on q alone. In Southeast Asia, strong temporal synchronization with squid-jigging activity but limited spatial explanatory power indicates that temporal agreement does not necessarily translate into complete spatial representation. This pattern is consistent with potential gaps in public vessel-tracking coverage, although the present data cannot distinguish incomplete AIS coverage from regional fleet composition or other differences between optical and tracking observations. The MaxEnt matching rates are interpreted separately as measures of model-observation agreement and are not used to assess AIS representativeness. VIIRS–DNB therefore provides a complementary optical signal for examining fishing patterns that are weakly represented in public AIS data.

In East Asia, the lower agreement between predicted high-potential zones and observed fishing-light locations indicates that the selected environmental predictors do not fully represent the observed distribution. The contrast between the two regions shows that the same remote-sensing framework can support different tasks: identifying potential AIS-based observation gaps in Southeast Asia and evaluating model-observation agreement in East Asia. The framework therefore supports region-specific fisheries monitoring and environmental interpretation.

4.3. Limitations and Future Remote-Sensing Applications

Although this study integrates multi-source observations, interpretation of the results is subject to three main sources of uncertainty: observation uncertainty, model uncertainty, and limited temporal coverage.

First, observation uncertainty arises from uneven AIS coverage [3–6] and residual limitations in VIIRS–DNB detection. Small-scale or weakly tracked vessels may be underrepresented in public AIS, whereas VIIRS–DNB detects radiance rather than vessel identity and nearshore detections may be affected by residual cloud and lunar contamination, coastal-light contamination, differences in vessel-light intensity, spatial resolution, and empirical threshold selection [7–9]. Accordingly, AIS–VIIRS comparisons should be interpreted as cross-source correspondence rather than a census of all fishing activity.

Second, model uncertainty limits the interpretation of the environment-based results. MaxEnt estimates environmental associations under presence-only sampling and the selected predictor set; the resulting patterns should therefore be interpreted as model-inferred associations rather than causal estimates of realized fishing suitability [28–30]. Spatial sampling, spatial autocorrelation, predictor collinearity, and omitted socioeconomic, operational, and management factors may influence the estimates. Because no separate correlation or VIF screening was conducted before model fitting, the relative contributions of individual predictors should be interpreted jointly within the selected predictor set rather than as independent effects. Moreover, the model used a random 75/25 training-validation split rather than spatially blocked validation, so nearby samples could occur in both subsets and the reported AUC values may be optimistic with respect to spatial transferability.

Finally, the 2017–2020 study period limits inference about post-2020 changes. Future work could evaluate the sensitivity of the results to VIIRS preprocessing, AIS coverage, spatial sampling, and model settings, and extend the framework with SAR observations, socioeconomic and management variables, and post-2020 data.

5. Conclusions

VIIRS–DNB revealed continuous, high-intensity fishing-light belts with summer–autumn peaks in East Asia, compared with more fragmented patterns and an earlier spring peak in Southeast Asia. AIS–VIIRS correspondence varied by region, vessel type, and metric; in Southeast Asia, strong temporal synchronization of squid-jigging activity coexisted with limited spatial explanatory power ($q = 7.8\%$). Within the selected predictor set, SST had the highest model-derived contribution in East Asia and SSS in Southeast Asia; these results represent environmental associations under presence-only sampling rather than causal drivers or direct measures of fishing suitability. Interpretation of the overall findings remains subject to uncertainties associated with AIS coverage, VIIRS detection and preprocessing, spatial sampling, predictor dependence, and the restriction of the analysis to 2017–2020.

https://doi.org/10.3390/su18178881

Author Contributions: L.C.: conceptualization, data curation, data preprocessing, formal analysis, spatial and statistical analysis, visualization, writing—original draft. C.W.: methodology, data curation, data preprocessing, spatial and statistical analysis, visualization, writing—review and editing. G.L.: data curation, formal analysis, spatial and statistical analysis, visualization, writing—review and editing. Z.L.: methodology. Z.C.: writing—review and editing. Q.Z.: writing—review and editing. Z.W.: supervision, writing—review and editing. Z.Y.: writing—review and editing. Z.Z.: conceptualization, study protocol development, supervision, writing—review and editing, funding acquisition. All authors have read and agreed to the published version of the manuscript.

Funding: The research was supported by the Open Research Fund Program of the Technology Innovation Center for South China Sea Remote Sensing, Surveying and Mapping Collaborative Application, Ministry of Natural Resources, China (No: RSSMCA-2024-B007) and National Natural Science Foundation of China (NSFC) (No: 42401432, No: 42571537).

Institutional Review Board Statement: Not applicable.

Informed Consent Statement: Not applicable.

Data Availability Statement: The raw input data used in this study are publicly available from the NOAA Earth Observation Group, Global Fishing Watch, and the Copernicus Marine Service. Processed datasets generated during the current study are not publicly shared at this stage because they are being used in ongoing follow-up work; they may be made available from the corresponding author upon reasonable request.

Acknowledgments: During the preparation of this manuscript, the authors used ChatGPT 5.6 Sol for basic grammar checking and language polishing only. The authors have reviewed and edited the output and take full responsibility for the content of this publication.

Conflicts of Interest: The authors declare no conflicts of interest.

Abbreviations

The following abbreviations are used in this manuscript:

AIS	Automatic Identification System
VIIRS–DNB	Visible Infrared Imaging Radiometer Suite Day/Night Band
FLB	Fishing-Light Brightness
FTD	Fishing-Track Density
KDE	Kernel Density Estimation
EHSA	Emerging Hot-Spot Analysis
SDI	Spatial Differentiation Index
SEM	Spatial Error Model
GD	Geodetector
SST	Sea-Surface temperature
SSS	Sea-Surface salinity
SSH	Sea-Surface height
SSV-U/V	Zonal and Meridional Surface-Current Velocity
DO	Dissolved Oxygen
MLD	Mixed-Layer Depth
Chl-a	Chlorophyll-a
AUC	Area Under the Receiver Operating Characteristic Curve
HPZ	High-Potential Zone
CMEMS	Copernicus Marine Environment Monitoring Service
GFW	Global Fishing Watch
EEZ	Exclusive Economic Zone
FAO	Food and Agriculture Organization

References

1. Wang, D.; Zheng, W.; Tang, S.; Zhang, L.; Liu, Y.; Yu, J. Nighttime Remote Sensing Analysis of Lit Fishing Boats: Fisheries Management Challenges in the South China Sea (2013–2022). *Remote Sens.* **2025**, *17*, 2967. [CrossRef]
2. Demanèche, S.; Bachiller, E.; Adamowicz, M.; Mugerza, E.; Vasconcelos, R.P.; Kovsars, M.; Egekvist, J.; Armstrong, M.; Bekaert, K.; Canha, Â.; et al. Relevance of European small-scale fisheries trapped by data limitations. *ICES J. Mar. Sci.* **2025**, *82*, fsaf130. [CrossRef]
3. McCauley, D.J.; Woods, P.; Sullivan, B.; Bergman, B.; Jablonicky, C.; Roan, A.; Hirshfield, M.; Boerder, K.; Worm, B. Ending hide and seek at sea. *Science* **2016**, *351*, 1148–1150. [CrossRef]
4. Kroodsma, D.A.; Mayorga, J.; Hochberg, T.; Miller, N.A.; Boerder, K.; Ferretti, F.; Wilson, A.; Bergman, B.; White, T.D.; Block, B.A.; et al. Tracking the global footprint of fisheries. *Science* **2018**, *359*, 904–908. [CrossRef]
5. Paolo, F.S.; Kroodsma, D.; Raynor, J.; Hochberg, T.; Davis, P.; Cleary, J.; Marsaglia, L.; Orofino, S.; Thomas, C.; Halpin, P. Satellite mapping reveals extensive industrial activity at sea. *Nature* **2024**, *625*, 85–91. [CrossRef]
6. Tassetti, A.; Galdelli, A.; Pulcinella, J.; Mancini, A.; Bolognini, L. Addressing gaps in small-scale fisheries: A low-cost tracking system. *Sensors* **2022**, *22*, 839. [CrossRef]
7. Zhao, M.; Zhou, Y.; Li, X.; Cao, W.; He, C.; Yu, B.; Li, X.; Elvidge, C.D.; Cheng, W.; Zhou, C. Applications of satellite remote sensing of nighttime light observations: Advances, challenges, and perspectives. *Remote Sens.* **2019**, *11*, 1971. [CrossRef]
8. Elvidge, C.D.; Ghosh, T.; Baugh, K.; Zhizhin, M.; Hsu, F.C.; Katada, N.S.; Penalosa, W.; Hung, B.Q. Rating the effectiveness of fishery closures with Visible Infrared Imaging Radiometer Suite boat detection data. *Front. Mar. Sci.* **2018**, *5*, 132. [CrossRef]
9. Li, Q.; Su, F.; Wang, W. Research on oil and gas platform extraction technology based on VIIRS data. *J. Geo-Inf. Sci.* **2017**, *19*, 398–406.
10. Hsu, F.C.; Elvidge, C.D.; Baugh, K.; Zhizhin, M.; Ghosh, T.; Kroodsma, D.; Susanto, A.; Budy, W.; Sudarja, Y. Cross-matching VIIRS boat detections with vessel monitoring system tracks in Indonesia. *Remote Sens.* **2019**, *11*, 995. [CrossRef]
11. Li, X.; Xiao, Y.; Su, F.; Wu, W.; Zhou, L. AIS and VBD data fusion for marine fishing intensity mapping and analysis in the northern part of the South China Sea. *ISPRS Int. J. Geo-Inf.* **2021**, *10*, 277. [CrossRef]
12. Ruiz, J.; Caballero, I.; Navarro, G. Sensing the same fishing fleet with AIS and VIIRS: A seven-year assessment of squid jiggers in FAO major fishing area 41. *Remote Sens.* **2019**, *12*, 32. [CrossRef]
13. Kiyofuji, H.; Saitoh, S.I. Use of nighttime visible images to detect Japanese common squid Todarodes pacificus fishing areas and potential migration routes in the Sea of Japan. *Mar. Ecol. Prog. Ser.* **2004**, *276*, 173–186. [CrossRef]
14. Zhang, C.; Chen, Y.; Xu, B.; Xue, Y.; Ren, Y. The dynamics of the fishing fleet in China Seas: A glimpse through AIS monitoring. *Sci. Total Environ.* **2022**, *819*, 153150. [CrossRef]
15. Syah, A.F.; Inayah, Z.; Partadisastra, M.A.; Yehezkiel, R. Dissemination of angling vessels in the eastern Indian Ocean: A remote sensing perspective. *IOP Conf. Ser. Earth Environ. Sci.* **2020**, *584*, 012053. [CrossRef]
16. Tian, H.; Liu, Y.; Tian, Y.J.; Liu, S.G.; Yan, L.X.; Chen, G.Y.; Li, J.C.; Li, Y.; Lin, L.S. Detection of Pacific saury (*Cololabis saira*) fishing boats in the Northwest Pacific using satellite nighttime imaging data. *J. Fish. China* **2019**, *43*, 2360–2371.
17. Huang, W.; Li, Y.; Yu, J.; Chen, G. Spatial distribution of light falling-net fishery vessels and its relationship with the ocean vortex in the northwestern Luzon Island based on remote sensing. *Haiyang Xuebao* **2018**, *40*, 10–19.
18. Long, Z.; Zuo, G.; Zhang, T.; Zheng, J. Exploring nighttime fishing and its impact factors in the northwestern South China Sea for sustainable fisheries. *Sustainability* **2025**, *17*, 8641. [CrossRef]
19. Food and Agriculture Organization of the United Nations. FAO Major Fishing Areas for Statistical Purposes. Available online: https://www.fao.org/cwp-on-fishery-statistics/handbook/general-concepts/main-water-areas/en/ (accessed on 20 August 2026).
20. Huang, C.; Kong, J.; Zheng, J.; Chen, Y.; Zhou, J. A novel framework for identifying fishing grounds from AIS data containing vessels of unknown types. *Front. Mar. Sci.* **2025**, *12*, 1576779. [CrossRef]
21. *GB/T 5147–2003*; The Classification, Nomenclature and Code of Fishing Gear. General Administration of Quality Supervision, Inspection and Quarantine of the People's Republic of China. Beijing, China, 2003.
22. Silverman, B.W. *Density Estimation for Statistics and Data Analysis*; Routledge: London, UK, 2018.
23. Getis, A.; Ord, J.K. The analysis of spatial association by use of distance statistics. *Geogr. Anal.* **1992**, *24*, 189–206. [CrossRef]
24. Yue, S.; Wang, C. The Mann-Kendall test modified by effective sample size to detect trend in serially correlated hydrological series. *Water Resour. Manag.* **2004**, *18*, 201–218. [CrossRef]
25. An, S.; Chang, R. Dynamics of spatial relation between producer services and manufacturing in coastal area of China. *China Soft Sci.* **2017**, *11*, 101–110.
26. Chen, A. *Spatial Econometrics: An Introduction with GeoDa Software Applications*; Zhejiang University Press: Hangzhou, China, 2014.
27. Wang, J.F.; Li, X.H.; Christakos, G.; Liao, Y.L.; Zhang, T.; Gu, X.; Zheng, X.Y. Geographical detectors-based health risk assessment and its application in the neural tube defects study of the Heshun Region, China. *Int. J. Geogr. Inf. Sci.* **2010**, *24*, 107–127. [CrossRef]

28. Phillips, S.J.; Dudík, M. Modeling of species distributions with Maxent: New extensions and a comprehensive evaluation. *Ecography* **2008**, *31*, 161–175. [CrossRef]
29. Phillips, S.J.; Anderson, R.P.; Schapire, R.E. Maximum entropy modeling of species geographic distributions. *Ecol. Model.* **2006**, *190*, 231–259. [CrossRef]
30. Fielding, A.H.; Bell, J.F. A review of methods for the assessment of prediction errors in conservation presence/absence models. *Environ. Conserv.* **1997**, *24*, 38–49. [CrossRef]
31. Liu, G.Y.; Wu, Z.F.; Wu, B.; Zheng, Z.; Cao, Z. Spatial and temporal characterization of global squid fishing in 2020. *J. Geo-Inf. Sci.* **2024**, *26*, 1110–1122.
32. Zhang, C.; Zhou, W.F.; Tang, F.H.; Shi, Y.; Fan, W. Forecasting models for yellowfin tuna fishing ground in the central and western Pacific based on machine learning. *Trans. Chin. Soc. Agric. Eng.* **2022**, *38*, 330–338.
33. Belkin, I.M.; Cornillon, P.C.; Sherman, K. Fronts in large marine ecosystems. *Prog. Oceanogr.* **2009**, *81*, 223–236. [CrossRef]
34. Qiu, B. Kuroshio and Oyashio currents. In *Encyclopedia of Ocean Sciences*, 3rd ed.; Cochran, J.K., Bokuniewicz, H.J., Yager, P.L., Eds.; Academic Press: Oxford, UK, 2019; pp. 384–394.
35. Fang, G.; Wang, Y.; Wei, Z.; Fang, Y.; Qiao, F.; Hu, X. Interocean circulation and heat and freshwater budgets of the South China Sea based on a numerical model. *Dyn. Atmos. Ocean.* **2009**, *47*, 55–72. [CrossRef]

https://doi.org/10.3390/su18178881